Bulletin of the Seismological Society of America, Vol. 103, No. 4, pp. 2151–2160, August 2013, doi: 10.1785/0120120224

Three-Dimensional Seismic-Wave Gradiometry for Scalar Waves

by Christian Poppeliers, Predrag Punoševac, and Tammy Bell

Abstract Wave gradiometry relates the spatial gradients of a wavefield to its velocity and radiation patterns through two spatial coefficients for any dimension. One coefficient gives the slowness of the wave in any given dimension, and the other coefficient gives the change in amplitude as a function of position and direction along the wavefront. In this paper, we develop the mathematical foundations for scalar wave gradiometry in three dimensions, building on previous work in 1D and 2D wave gradiometry. We validate our method by synthetic tests and find that our method can accurately estimate wave direction and speed. Estimating spatial amplitude changes is not as robust, however. Numerical tests indicate that the wave gradiometry method is highly sensitive to uncorrelated noise in the data as well as the presence of interfering waves.

Introduction

Array analysis of time series data is designed to extract wave attributes from a propagating wavefield (Rost and Thomas, 2002). For example, the seismology community has relied heavily on array analysis to provide information on a seismic wavefield's direction and speed while also assisting in the identification of seismic arrivals from deep earth targets (Earle *et al.*, 2011). Recording and analysis of seismic array data can also help to discriminate between earthquakes and explosions as sources of seismic waves (Selby, 2011).

Typically, seismic arrays are designed such that the aperture is tens to hundreds of times larger than the central wavelength being analyzed and the average station spacing is on the order of a single wavelength. Such a geometry translates into an array that can be tens to hundreds of kilometers in aperture (Frosch and Green, 1966; Kay *et al.*, 1999). A new paradigm of array processing relies on an array that has an aperture of $< 10\%$ of the wavefield's central wavelength with an average station spacing of only a few percent of the wavelength. This type of array, referred to as a gradiometer, will typically have an aperture of less than a hundred meters for regional seismic studies to only a few meters for local seismic studies (Langston *et al.*, 2006; Langston, 2007a,b,c; Langston and Liang, 2008; Liang and Langston, 2009; Poppeliers, 2010, 2011). This type of phased array processing, referred to as seismic gradiometry or seismic gradiometric analysis, relies on the relationship between the spatial gradients of the wave, its time derivative, and the wave's propagation velocity.

Conventional seismic array processing has the goal of resolving average wave slowness over a specified time window. Because an array is deployed in a 2D configuration onto the ground, however, the data analysis can only resolve the slowness vectors as projected onto the horizontal surface (e.g., the ground). It would be a great step forward if the analysis could estimate the 3D slowness vector, which would be possible if the array were configured in three dimensions. The principle obstacle to deploying a conventional 3D array, however, is that such an array would be too large. Specifically, to resolve a seismic wavefield's propagation characteristics one would have to deploy seismic instruments in boreholes several tens to hundreds of kilometers deep, which is prohibitively expensive and in some cases technically impossible. This is the advantage of gradiometric analysis; because the gradiometer needs to be quite small, it becomes technically tractable and economically feasible to deploy a 3D gradiometer.

The mathematical foundations of gradiometry have been developed for scalar and polarized waves in one and two dimensions (Langston *et al.*, 2006; Langston, 2007a,b,c). In this paper we develop the mathematical foundations of 3D gradiometry for scalar waves and validate our methodology using numerical tests. We also explore the effects of both uncorrelated noise and interfering wavefields on the efficacy of our method.

Spatial Gradient Theory in Three Dimensions

The basic gradiometry problem in three dimensions can be solved as three 1D problems, as was pointed out in Langston (2007c). When taking this approach, the analysis relates two wave parameters A and B that are related to the wave's vector slowness and the wave's spatial amplitude change.

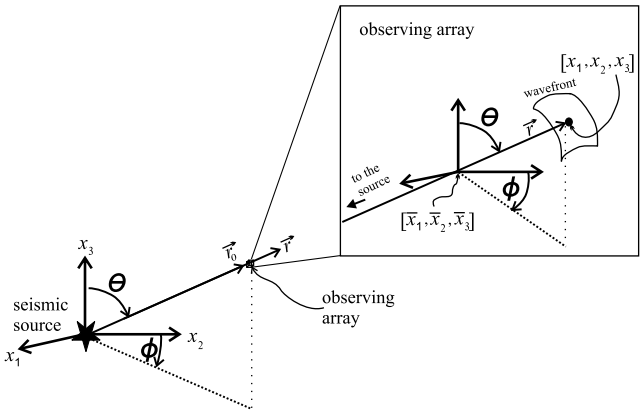

Figure 1. The coordinate system used to define the problem is centered at the seismic source, and the derivations assume a spherical wave. The quantity $\vec{r}_0$ denotes the vector from the seismic source to the center of the recording array, and $\vec{r}$ is the vector from the source to a point on the wavefront and parallel to $\vec{r}_0$. The array center is located at point $[\bar{x}_1, \bar{x}_2, \bar{x}_3]$. The gray axes are oriented in the same direction as the source-centered coordinate system $[x_1, x_2, x_3]$.

Geometrical Spreading and Radiation Pattern in Three Dimensions

For our model, we assume a spherical wave radiating outwards from the source in a homogeneous medium. Although this is not strictly accurate for actual seismic waves that propagate through the heterogeneous Earth, this first-order approximation significantly simplifies the derivation that follows. We center a Cartesian coordinate system $[x_1, x_2, x_3]$ at the seismic source and designate the coordinates of the center of the recording array as $[\bar{x}_1, \bar{x}_2, \bar{x}_3]$. The quantity $\vec{r}_0$ is a vector from the seismic source to the center of the array, and $\vec{r}$ is a vector from the seismic source to the point on the wavefront and is parallel to $\vec{r}_0$. The angle ϕ is measured clockwise from the x_2 axis to the projection of $\vec{r}$ onto a horizontal surface, and the angle θ is measured from the x_3 axis to $\vec{r}$. Note that, with this model, $\vec{r}$ is perpendicular to the local wavefront as it traverses the array (Fig. 1). Following work from 1D and 2D wave gradiometry, we assume that a spherical wave propagates across the array at location (r, θ, ϕ), where r is the scalar distance from the seismic source to the wavefront ($r = |\vec{r}|$). The form of the wave is

$$u_s(t, r, r_0, \theta, \phi) = G_s(r) R_s(\theta, \phi) f[t - |\vec{p}|(r)(r - r_0)], \quad (1)$$

where $G_s(r)$ is the geometrical spreading of the wavefront and $R_s(\theta, \phi)$ is the spatial amplitude changes in the θ and ϕ directions. The term $f[t - |\vec{p}|_s(r)(r - r_0)]$ represents the phase variation as a function of time t and location r relative to the center of the array $r - r_0$, with $|\vec{p}_s(r)|$ the wavespeed. The subscript s is a parameter in these quantities and represents the time of arrival of a given wave at the array. The radial and azimuthal derivatives are

$$\begin{bmatrix} \frac{\partial u_s}{\partial r} \\ \frac{\partial u_s}{\partial \theta} \\ \frac{\partial u_s}{\partial \phi} \end{bmatrix} = u_s \begin{bmatrix} A_s(r) \\ \frac{1}{R_s(\theta,\phi)} \frac{\partial R_s(\theta,\phi)}{\partial \theta} \\ \frac{1}{R_s(\theta,\phi)} \frac{\partial R_s(\theta,\phi)}{\partial \phi} \end{bmatrix} + \frac{\partial u_s}{\partial t} \begin{bmatrix} B_s(r) \\ 0 \\ 0 \end{bmatrix}, \quad (2)$$

where the radial coefficients are

$$A_s(r) = \frac{1}{G_s(r)} \frac{\partial G_s(r)}{\partial r}, \quad (3)$$

and

$$B_s(r) = -\left[p_s(r) + \frac{\partial p_s(r)}{\partial r}(r - r_0) \right]. \quad (4)$$

The term $A_s(r)$ describes the amplitude change as a function of radial distance from the source, and $B_s(r)$ is related to wave velocity. Note that equation (2) is an equation on a family of functions, one for each wave arrival time s (Langston, 2007b).

Seismic data are measured in the Cartesian coordinates, but the 3D gradiometry problem is most easily cast in spherical coordinates. Thus, we begin by relating the two coordinate systems with the well known mapping:

$$x_1 = r \sin\theta \sin\phi \qquad x_2 = r \sin\theta \cos\phi \qquad x_3 = r \cos\theta. \quad (5)$$

Combining equations (1) and (5) and using the chain rule of calculus allows us to write the spherical derivatives in terms of the Cartesian quantities:

$$\frac{1}{r} \begin{bmatrix} r \frac{\partial u_s}{\partial r} \\ \frac{\partial u_s}{\partial \theta} \\ \frac{\partial u_s}{\partial \phi} \end{bmatrix} = \mathbf{Q} \begin{bmatrix} \frac{\partial u_s}{\partial x_1} \\ \frac{\partial u_s}{\partial x_2} \\ \frac{\partial u_s}{\partial x_3} \end{bmatrix}, \quad (6)$$

where

$$\mathbf{Q} = \begin{bmatrix} \sin\theta \sin\phi & \sin\theta \cos\phi & \cos\theta \\ \cos\theta \sin\phi & \cos\theta \cos\phi & -\sin\theta \\ \sin\theta \cos\phi & -\sin\theta \sin\phi & 0 \end{bmatrix}. \quad (7)$$

Now assume the Cartesian form of a displacement wave traversing the array as

$$u_s(t, x_1, x_2, x_3) = H_s(x_1, x_2, x_3) \times f[t - p_s(x_1)(x_1 - \bar{x}_1) - p_s(x_2)(x_2 - \bar{x}_2) - p_s(x_3)(x_3 - \bar{x}_3)], \quad (8)$$

where $[\bar{x}_1, \bar{x}_2, \bar{x}_3]$ is the center of the gradiometer and the spatial amplitude changes are given by $H_s(x_1, x_2, x_3)$, which relates to $G_s(r) R_s(\theta, \phi)$. Because different waves can arrive at different times s and directions, we denote the slowness components as $p_s(x_i)$ where $i = 1, 2, 3$ denotes the component direction.

Following the approach of Langston (2007a,b,c), we differentiate equation (8) with respect to x_1, x_2, and x_3;

$$\begin{bmatrix} \frac{\partial u_s}{\partial x_1} \\ \frac{\partial u_s}{\partial x_2} \\ \frac{\partial u_s}{\partial x_3} \end{bmatrix} = u_s \begin{bmatrix} A_s(x_1) \\ A_s(x_2) \\ A_s(x_3) \end{bmatrix} + \frac{\partial u_s}{\partial t} \begin{bmatrix} B_s(x_1) \\ B_s(x_2) \\ B_s(x_3) \end{bmatrix}, \tag{9}$$

where

$$\begin{aligned} A_s(x_1) &= \frac{1}{H_s(x_1,x_2,x_3)} \frac{\partial H_s(x_1,x_2,x_3)}{\partial x_1} \\ A_s(x_2) &= \frac{1}{H_s(x_1,x_2,x_3)} \frac{\partial H_s(x_1,x_2,x_3)}{\partial x_2} \\ A_s(x_3) &= \frac{1}{H_s(x_1,x_2,x_3)} \frac{\partial H_s(x_1,x_2,x_3)}{\partial x_3} \end{aligned} \tag{10}$$

and

$$\begin{aligned} B_s(x_1) &= -\left[p_s(x_1) + \frac{\partial p_s(x_1)}{\partial x_1}(x_1 - \bar{x}_1) \right] \\ B_s(x_2) &= -\left[p_s(x_2) + \frac{\partial p_s(x_2)}{\partial x_2}(x_2 - \bar{x}_2) \right] \\ B_s(x_3) &= -\left[p_s(x_3) + \frac{\partial p_s(x_3)}{\partial x_3}(x_3 - \bar{x}_3) \right]. \end{aligned} \tag{11}$$

Combining (6) and (9) we get

$$\frac{1}{r} \begin{bmatrix} r\frac{\partial u_s}{\partial r} \\ \frac{\partial u_s}{\partial \theta} \\ \frac{\partial u_s}{\partial \phi} \end{bmatrix} = u_s \mathbf{Q} \begin{bmatrix} A_s(x_1) \\ A_s(x_2) \\ A_s(x_3) \end{bmatrix} + \frac{\partial u_s}{\partial t} \mathbf{Q} \begin{bmatrix} B_s(x_1) \\ B_s(x_2) \\ B_s(x_3) \end{bmatrix}. \tag{12}$$

Combining equations (12) with equations (2)–(4) gives us the first result of this section:

$$\begin{bmatrix} rA_s(r) \\ \frac{1}{R_s(\theta,\phi))} \frac{\partial R_s(\theta,\phi)}{\partial \theta} \\ \frac{1}{R_s(\theta,\phi))} \frac{\partial R_s(\theta,\phi)}{\partial \phi} \end{bmatrix} = r\mathbf{Q} \left(\begin{bmatrix} A_s(x_1) \\ A_s(x_2) \\ A_s(x_3) \end{bmatrix} + \frac{1}{u_s} \frac{\partial u_s}{\partial t} \begin{bmatrix} B_s(x_1) \\ B_s(x_2) \\ B_s(x_3) \end{bmatrix} \right) - \frac{1}{u_s} \frac{\partial u_s}{\partial t} \begin{bmatrix} rB_s(r) \\ 0 \\ 0 \end{bmatrix}. \tag{13}$$

Equation (13) relates the spatial amplitude changes to the spatial and temporal derivatives and the direction of the recorded wavefield. The first equation gives $A_s(r)$, which is the geometrical spreading for a wave arriving at time s:

$$\begin{aligned} A_s(r) = &\left[A_s(x_1) + \frac{1}{u_s}\frac{\partial u_s}{\partial t} B_s(x_1) \right] \sin\theta \sin\phi \\ &+ \left[A_s(x_2) + \frac{1}{u_s}\frac{\partial u_s}{\partial t} B_s(x_2) \right] \sin\theta \cos\phi \\ &+ \left[A_s(x_3) + \frac{1}{u_s}\frac{\partial u_s}{\partial t} B_s(x_3) \right] \cos\theta - \frac{1}{u_s}\frac{\partial u_s}{\partial t} B_s(r). \end{aligned} \tag{14}$$

The second two equations

$$\begin{aligned} \frac{1}{R_s(\theta,\phi)} \frac{\partial R_s}{\partial \theta} = r\Bigg[&\left(A_s(x_1) + \frac{1}{u_s}\frac{\partial u_s}{\partial t} B_s(x_1) \right) \cos\theta \sin\phi \\ &+ \left(A_s(x_2) + \frac{1}{u_s}\frac{\partial u_s}{\partial t} B_s(x_2) \right) \cos\theta \cos\phi \\ &- \left(A_s(x_3) + \frac{1}{u_s}\frac{\partial u_s}{\partial t} B_s(x_3) \right) \sin\theta \Bigg] \end{aligned} \tag{15}$$

and

$$\begin{aligned} \frac{1}{R_s(\theta,\phi)} \frac{\partial R_s}{\partial \phi} = r\Bigg[&\left(A_s(x_1) + \frac{1}{u_s}\frac{\partial u_s}{\partial t} B_s(x_1) \right) \sin\theta \cos\phi \\ &- \left(A_s(x_2) + \frac{1}{u_s}\frac{\partial u_s}{\partial t} B_s(x_2) \right) \sin\theta \sin\phi \Bigg] \end{aligned} \tag{16}$$

give the spatial change in amplitude along the wavefront in the θ and ϕ directions, respectively.

To estimate the geometrical spreading $A_s(r)$, one only has to estimate the parameters $A_s(x_i)$, $B_s(x_i)$ (where $i = 1, 2, 3$), and the time derivative of the recorded wavefield for all arrival times s on the seismogram. Note that the wave direction is estimated from the $B_s(x_i)$, which is described in the next section. Estimating the radiation pattern $R_s(\theta, \phi)$, however, is not as straightforward. Dividing equation (15) by equation (16) gives us the second result of this section:

$$\frac{\frac{\partial R_s}{\partial \theta}}{\frac{\partial R_s}{\partial \phi}} = \frac{J_1(\theta,\phi)}{J_2(\theta,\phi)},$$

that is,

$$J_2(\theta,\phi)\frac{\partial R_s}{\partial \theta} - J_1(\theta,\phi)\frac{\partial R_s}{\partial \phi} = 0, \tag{17}$$

where

$$\begin{aligned} J_1 = &[A_s(x_1)\cos\theta\sin\phi + A_s(x_2)\cos\theta\cos\phi - A_s(x_3)\sin\theta] \\ &+ \frac{1}{u_s}\frac{\partial u_s}{\partial t}[B_s(x_1)\cos\theta\sin\phi + B_s(x_2)\cos\theta\cos\phi \\ &- B_s(x_3)\sin\theta] \end{aligned} \tag{18}$$

and

$$\begin{aligned} J_2 = &[A_s(x_1)\sin\theta\cos\phi - A_s(x_2)\sin\theta\sin\phi] \\ &+ \frac{1}{u_s}\frac{\partial u_s}{\partial t}[B_s(x_1)\sin\theta\cos\phi - B_s(x_2)\sin\theta\sin\phi]. \end{aligned} \tag{19}$$

In principle, the linear partial differential equation (17) can be solved numerically. Specifically, one could set up a system of equations where the J_1 and J_2 are determined for a

range of wave directions θ and ϕ. One could then fit an assumed radiation pattern to the data to solve for the parameters of the moment tensor (e.g., strike, dip, and rake). In the case of a single gradiometer, however, the problem is ill posed and inversion would not return meaningful results. Solving for the radiation pattern would take several simultaneous gradiometer deployments to more fully sample the wavefield and is outside the scope of this paper. We address the solution of equation (17), however, in a forthcoming paper.

Implementing 3D Spatial Gradient Analysis

To resolve wave attributes, we use a phased array to measure the wavefield and estimate the corresponding spatial derivatives for all points on the seismogram. From the spatial derivatives, we can determine the parameters A_s and B_s, which can then be used to determine the wave attributes for every point along the seismograms. The simplest way to estimate wavefield spatial gradients is via a finite-difference formulation (Langston, 2007c, equations 47–50). The finite-difference formulation requires a uniform station distribution, however. A more flexible approach is to use arbitrarily placed stations and estimate the spatial gradients in a least-squares sense. Specifically, given N seismic stations in a 3D array, we compute the spatial gradient $du_s^{\{k\}}$ at location $r^{\{k\}} = [x_1^{\{k\}}, x_2^{\{k\}}, x_3^{\{k\}}]$ for all arrival times s relative to the master station $r^{\{0\}} = [x_1^{\{0\}}, x_2^{\{0\}}, x_3^{\{0\}}]$ by expanding the Taylor series:

$$\begin{aligned} du_s^{\{k\}} &= u_s^{\{k\}} - u_s^{\{0\}} \\ &= \delta x_1^{\{k\}} \frac{\partial u_s}{\partial x_1} + \delta x_2^{\{k\}} \frac{\partial u_s}{\partial x_2} + \delta x_3^{\{k\}} \frac{\partial u_s}{\partial x_3} + du_{s,\mathrm{err}}^{\{k\}}, \end{aligned} \quad (20)$$

where the time dependence of the seismograms is implied by the subscript s. Neglecting the error term we can rewrite equation (20) as a matrix equation

$$\begin{bmatrix} u_s^{\{1\}} - u_s^{\{0\}} \\ u_s^{\{2\}} - u_s^{\{0\}} \\ \vdots \\ u_s^{\{N\}} - u_s^{\{0\}} \end{bmatrix} = \begin{bmatrix} \delta x_1^{\{1\}} & \delta x_2^{\{1\}} & \delta x_3^{\{1\}} \\ \delta x_1^{\{2\}} & \delta x_2^{\{2\}} & \delta x_3^{\{2\}} \\ \vdots & \vdots & \vdots \\ \delta x_1^{\{N\}} & \delta x_2^{\{N\}} & \delta x_3^{\{N\}} \end{bmatrix} \begin{bmatrix} \frac{\partial u_s}{\partial x_1} \\ \frac{\partial u_s}{\partial x_2} \\ \frac{\partial u_s}{\partial x_3} \end{bmatrix} \quad (21)$$

(Liang and Langston, 2009). The term on the left side is a vector containing the waveform variations relative to the master station, the $3 \times N$ matrix contains the gradiometer geometry, and the 1×3 vector on the right side contains the spatial gradients in the three-component directions $[x_1, x_2, x_3]$. By solving equation (21) via standard matrix inversion techniques, we obtain the spatial derivatives of the wavefield for a given time point s.

The advantage of this approach is that the station spacing can be nonuniform and an arbitrary number of stations can be used, so long as the array is 3D in its structure. In practice, it would be desirable to use as many stations as practical, as there is a significant averaging effect in the least-squares solution of equation (21). Thus, a single spurious station would not have a significantly deleterious effect on the estimation of the gradient. Also, having numerous stations allows the freedom to eliminate stations with suspect data so long as the array maintains its 3D structure. Once the gradients are estimated, we can compute coefficients $B_s(x_1)$, $B_s(x_2)$, $B_s(x_3)$, $A_s(x_1)$, $A_s(x_2)$ and $A_s(x_3)$ for every point (i.e., for all arrival times s) on the seismogram using the time-domain implementation described in (Langston, 2007b), which we will not repeat here for brevity's sake.

Determining Wave Direction and Speed in Three Dimensions

To resolve ϕ_s and θ_s of the wave vector, we use the fact that $B_s(x_i) = -p_s(x_i)$, $i = 1, 2, 3$. That is, the $B_s(x_i)$ coefficient is directly related to the slowness in the component direction $i = 1, 2, 3$ of a wave arriving at time s. We can then define the wave azimuth ϕ_s as the projection of the wave vector onto a horizontal surface:

$$\phi_s = \tan^{-1}\left[\frac{B_s(x_1)}{B_s(x_2)}\right]. \quad (22)$$

Observe that equation (22) also follows from equations (2) and (12). Namely, from equation (2) it follows that $\frac{\partial u_s}{\partial \theta}$ cannot contain the velocity term. Thus, by multiplying the matrix $\mathbf{Q}$ with $[B_s(x_1), B_s(x_2), B_s(x_3)]^T$ in equation (12) we obtain the velocity component of $\frac{\partial u_s}{\partial \theta}$

$$B_s(x_1)\sin\theta\cos\phi - B_s(x_2)\sin\theta\sin\phi$$

which must be equal to zero; that is,

$$B_s(x_1)\sin\theta\cos\phi - B_s(x_2)\sin\theta\sin\phi = 0$$

which in turn gives equation (22).

The wave direction θ_s is defined as the angle between the wave vector and the x_3 axis:

$$\theta_s = \cos^{-1}\left[\frac{B_s(x_3)}{B_s(|\vec{r}|)}\right], \quad (23)$$

where

$$B_s(|\vec{r}|) = -p_s(|\vec{r}|) \quad (24)$$

is the wave slowness (inverse speed) and

$$p_s(|\vec{r}|) = \sqrt{p_s(x_1)^2 + p_s(x_2)^2 + p_s(x_3)^2}. \quad (25)$$

Numerical Tests

An important method of testing the validity of our algorithm is to attempt to recover wave-propagation parameters from a synthetic signal. Tests of this sort are instructive as they serve as a best-case scenario, where:

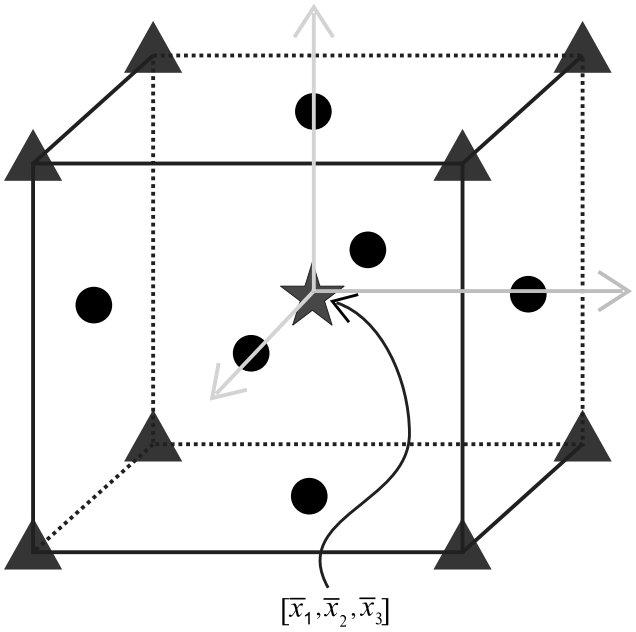

Figure 2. The configuration of the array used in the synthetic tests. The virtual sensor at the center of the cube served as the array's local origin and is located at the point $[\bar{x}_1, \bar{x}_2, \bar{x}_3]$. Additionally, sensors were placed on all corners of the array (triangles), as well as the centers of each cube face (dots).

1. the data is completely noise free;
2. the data obeys our simplified models of wave propagation;
3. we have prior knowledge of the wave parameters to compare against those estimated from our algorithm.

To conduct this test, we created a virtual, cubic, fifteen-element array with simulated seismometers located on the corners of the cube, as well as in the center of the cube and on each face (Fig. 2). The array aperture is ~60 m. For this work here, we simulate an isotropic point source (i.e., $R_s(\theta, \phi) =$ constant) with geometrical spreading. Thus, equation (8) can be rewritten as

$$u_s(t, x_1^{\{k\}}, x_2^{\{k\}}, x_3^{\{k\}}) = \frac{1}{|\vec{r}_k|} f[t - x_1^{\{k\}} p(x_1) - x_2^{\{k\}} p(x_2) - x_3^{\{k\}} p(x_3)], \quad (26)$$

where $(x_1^{\{k\}}, x_2^{\{k\}}, x_3^{\{k\}})$ is the kth station's array coordinates, $|\vec{r}_k|$ is the scalar distance between the seismic source and a station located at $(x_1^{\{k\}}, x_2^{\{k\}}, x_3^{\{k\}})$, and $p(x_1)$, $p(x_2)$, $p(x_3)$ are the (potentially time-varying) wave slownesses at the center of the array in the x_1, x_2, and x_3 directions, respectively. We assume that the wavespeed is uniform across the array. For the results presented here, we use a simple isotropic seismic source. We note, however, that when we use a more complicated radiation pattern in our synthetic tests, the results of our synthetic tests are virtually identical.

The function given by equation (26) simulates a spherically symmetric wave traveling through an infinite three space. For this work, we define $p(x_1)$, $p(x_2)$, $p(x_3)$ to be time variable (within the range of 0.0001 s/m and 0.0004 s/m) to test our method's ability to resolve time-varying wave direction and wavespeed. Given that our analytical model assumes a spherical wave with the coordinate system centered at the seismic source, it becomes a reasonable question as to how the wave velocity $\vec{p}$ can vary in time. One way to think about this contradiction is to remember that wave gradiometry will resolve the wave direction at each time point s of the wavefield as it traverses the array. The vector $\vec{r}$ is parallel to $\vec{p}$ in our model; therefore, the source must move in time. This gives us three possible interpretations. First, the source can truly move in time, as could be explained by a finite-fault rupture process or seismic scattering, where each scattering point acts as a source. Second, what we are calling the seismic source can be thought of as a pseudosource. The pseudosource is located along the constructed vector $\vec{r}$ at some distance r from the array, where $\vec{r}$ is parallel to $\vec{p}$. In other words, $\vec{r}$ is parallel to the local wave vector but not necessarily parallel to a vector connecting the actual source to the gradiometer: that is to say, the wavepath curves. Finally, it can be different arrivals (e.g., P and S) arriving at the array with differing slownesses.

For the time function $f(t)$ we used a seismogram recorded by station TA234A of USArray on 24 February 2010. To compute the seismogram at each array station located at $\vec{r}_k$, we first calculate the time shift at array station k as the dot product between the slowness vector and the vector describing the station's location:

$$\Delta t_k = \vec{p} \cdot (\vec{r}_k - \vec{r}), \quad (27)$$

where $\vec{p}$ is the potentially time-varying vector slowness $[p(x_1), p(x_2), p(x_3)]$. Note that because we use a time-variable slowness vector, equation (27) must be computed for all points along the function $f(t)$. Thus, each station k has a time-shifted version $f(t + \Delta t_k)$ where the time shift varies according to $\vec{p}$. Note that the seismogram $f(t + \Delta t_k)$ may not be equally sampled in time (due to the time-variable vector slowness), so we interpolate $f(t + \Delta t_k)$, using a cubic spline function, to a regular sample rate of 0.01 samples per second. After interpolation, we apply the geometrical spreading ($1/r$, where $r_k \approx 15$ km) and a 0.1–5 Hz, band-pass filter. This passband ensured that the array's nominal aperture is no greater than ~3% of a wavelength. We do this to minimize numerical errors associated with estimating the spatial derivatives (Langston, 2007c). Note that we use a highly variable slowness vector in constructing the synthetic data (Fig. 3). Although this type of wavefield is not likely to occur in nature, we do this to provide a vigorous test to our method's ability to resolve wave direction and speed.

Because of the potential divide-by-zeros issues in using the time domain method to estimate the A and B coefficients, we impose the same criteria as suggested in Langston

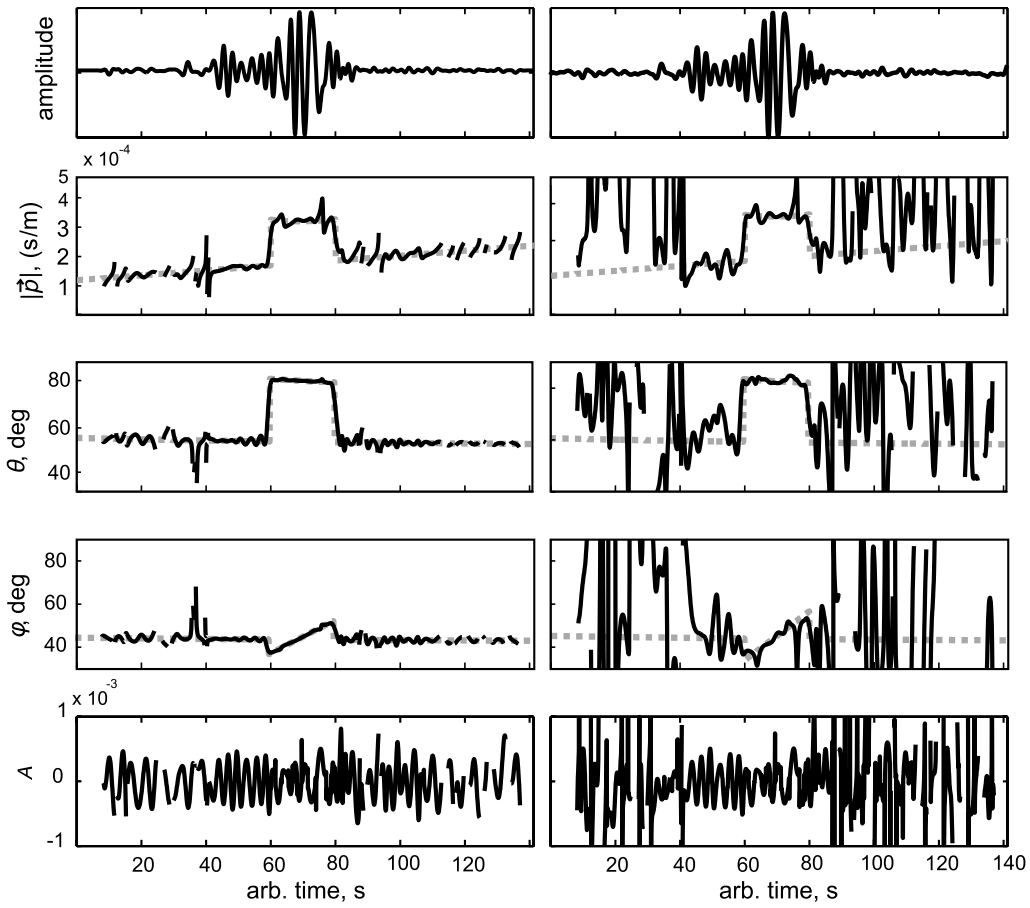

Figure 3. Results of gradiometric analysis on synthetic data. The top row of panels shows the synthetic seismograms as recorded by the center station of the array. The column on the left is for noise-free data, whereas the column on the right is for data that contains random, uncorrelated noise. For this figure, the noise takes the form of a time series of randomly distributed random numbers filtered to contain the same frequency content as the synthetic seismogram and has an rms amplitude that is 5% that of the synthetic seismogram. The next four rows of panels show the wave attribute estimates (solid black line) compared to actual, known wave attributes (dashed gray line). Note that there are regions where there is no estimate of a given wave parameter. This occurs when the amplitude of the signal and its envelope fall below a predefined criterion. This test returns estimates of the wave parameters that match the actual wave parameters, confirming the validity of our algorithm. This figure, however, also shows that the method is highly sensitive to uncorrelated noise. The step in the wave parameters between 60 and 80 s represents a change in slowness and serves to illustrate that our method can estimate wave parameters as a function of time.

(2007b). In essence, the amplitude of the signal and its corresponding envelope function must be a certain percentage of the respective maximum amplitudes (we chose a value of 0.1%). Increasing this number decreases the amount of signal analyzed.

Figure 3 shows the results of applying our method to noise-free synthetic data as well as to data with a small amount of additive, uncorrelated noise. The figure shows that our algorithm recovers the wave direction and slowness of the noise-free synthetic data, but with a certain degree of scatter. Specifically, for the low-amplitude portion of the noise-free signal (10 s $> t >$ 40 s) the estimated magnitude of slowness varies by as much as $\pm$15% about the actual value. For the higher amplitude portions of the signal (for example, $t \approx 70$ s), however, the degree of scatter decreases. The same scatter can be seen in the estimates of the wave direction. Because there is no noise for this test, the scatter can only be attributed to numerical errors in estimating the gradients (equation 21).

When a small amount of uncorrelated noise is present in the data (in this case, the noise has a root mean square [rms] amplitude of 5% of the rms amplitude of the data), the scatter in the wave parameter estimates is significantly increased. For this example, we added a unique noise signal to each seismogram and then filter the resulting signal to have a frequency content equal to that of the noise-free data. The rationale for filtering the noisy signal is that when processing actual data, any random noise component will be superposed onto the seismogram and filtered with the seismogram itself. Thus, the random noise will have a similar frequency range of the filtered seismogram.

Because the noise amplitude remains at an approximately constant rms amplitude for the entire seismogram, the signal-to-noise (SNR) ratio is variable for the signal.

Specifically, for the portions of the seismogram when the signal amplitude is high, the SNR is high as well. During these time windows, the scatter in wave-parameter estimates is significantly lower than during the low SNR portions of the signal, as would be expected. We provide this test as an illustration of the sensitivity of wave gradiometry to uncorrelated noise, and in the next section we expand this analysis.

We do not attempt to solve for the radiation pattern $R_s(\theta, \phi)$ here. As stated in the previous section, it is possible in principle to solve for $R_s(\theta, \phi)$; for a single gradiometer deployment, however, the problem would be too ill posed to yield a meaningful result.

Effects of Uncorrelated Noise

Uncorrelated noise can severely denigrate the accuracy of estimated wave parameters (Poppeliers, 2010, 2011). Typically, for gradiometry to return reliable estimates of wave parameters, the recording stations must be calibrated and the waveforms used in the analysis must be highly correlated. Although in this synthetic case we are assured that the waveforms are highly correlated and that station calibration is a moot point, we investigate the degree to which uncorrelated noise in the signal itself can impact the results. To explore this, we added random noise to each virtual seismometer in the array. The synthetic signal had a constant wave direction of $\phi = 45°$, $\theta = 53°$, $|\vec{p}| = 0.00011$ s/m where the source was located 15 km from the array. To form the noise, we created a vector of random numbers normally distributed between $-\Lambda 0.5$ to $\Lambda 0.5$, where Λ is a constant that controls the rms amplitude of the noise signal. The noise signal is unique, and thus uncorrelated, for each recording station in the array. We set the magnitude of Λ to a value between 0% and 20% of the signal's rms amplitude, add the noise to the signal, and then filter the resulting seismogram to 0.2–0.5 Hz. We then estimate the average wave parameter over a time window of 60–65 s and compute the standard deviation about the mean wave attribute for this time window. The averaged wave attribute is plotted against the magnitude of the noise as well as ± 1 standard deviation about the mean attribute. We use the standard deviation as a proxy for the uncertainty in the estimate of the given wave attribute. Because each noise realization is unique, each given test like this will yield unique results. We are interested in a statistical picture of how random noise can effect our results. Thus, we repeated the test one thousand times and averaged all the results, similar to commonly used Monte Carlo methods.

Figure 4 shows the results of the noise test for estimates of ϕ_s, θ_s, $|\vec{p}_s|$, and $A_s(r)$. As expected for zero noise amplitude, the scatter in the wave-parameter estimates (as quantified by the uncertainty) is nearly zero. As the rms amplitude of the noise increases, however, the uncertainty increases for all the estimated wave parameters. As expected, when the amplitude of the uncorrelated noise increases the degree of uncertainty in the estimated wave parameter also increases. Also, for the parameters ϕ_s, θ_s, and $|\vec{p}|$, the accuracy is negatively affected by uncorrelated noise. Although the degree of scatter (as measured by the standard deviation) increases differently for each wave parameter, the major point to be learned from these tests is that the wave parameter estimates are only reliable and stable when the rms amplitude of the uncorrelated noise is small. Clearly, the gradiometric method is very sensitive to noise.

Effects of Wave Interference

In the previous section, we considered the case where the noise was uncorrelated from instrument to instrument. A more realistic noise source, however, is one that is correlated across the array. An example of this may be the presence of a second wavefield arising from an actual seismic source. For example, a microseism wavefield and the wavefield from an earthquake could traverse the array simultaneously. Therefore, the question becomes: to what degree would the noise (e.g., a second, actual signal such as microseism) affect the results of gradiometric analysis? In this section, we use two superposed, synthetic wavefields in the attempt to answer this question. Specifically, we simulate microseism as a 0.1 Hz sinusoidal plane wave with $\phi_s = 45°$, $\theta_s = 0°$, and $|\vec{p}| = 0.0003$ s/m. This will be termed S_m. We add the S_m signal to the original signal, termed S_0, (with a constant $\phi_s = 130°$, $\theta_s = 35°$, and $|\vec{p}_s| = 0.00013$ s/m) at varying amplitudes, compute the resulting wave direction, speed, and geometrical spreading, average over the time interval of 60–65 s, and compute the standard deviation (Fig. 5).

The results of the test are as expected. For very low S_m amplitudes, the analysis returns the wave parameters of the S_0 signal. As the amplitude of S_m increases, however, the scatter in the wave parameters (as measured by the standard deviation) increases. As the amplitude of S_m continues to increase, the analysis eventually returns the wave parameters of the S_m signal itself, as it dominates the recorded signal. The details of how each wave parameter is affected by this type of coherent noise are summarized below.

Magnitude Slowness. The magnitude slowness quickly becomes inaccurate at S_m amplitudes of only a few percent. It is not until the S_m signal has an amplitude of 90% of the S_0 signal that the estimate of the magnitude slowness stabilizes to that of the S_m signal.

Direction. Similar to magnitude slowness, the directions θ and ϕ quickly become inaccurate at S_m amplitudes of only a few percent of the rms amplitude of S_0. At S_m amplitudes of $> 30\%$ of the S_0 amplitude, however, the direction estimates approach the values of the S_0 signal, and the degree of scatter rapidly decreases.

Geometrical Spreading. The geometrical spreading is the least robust of the wave parameters tested here, and this is

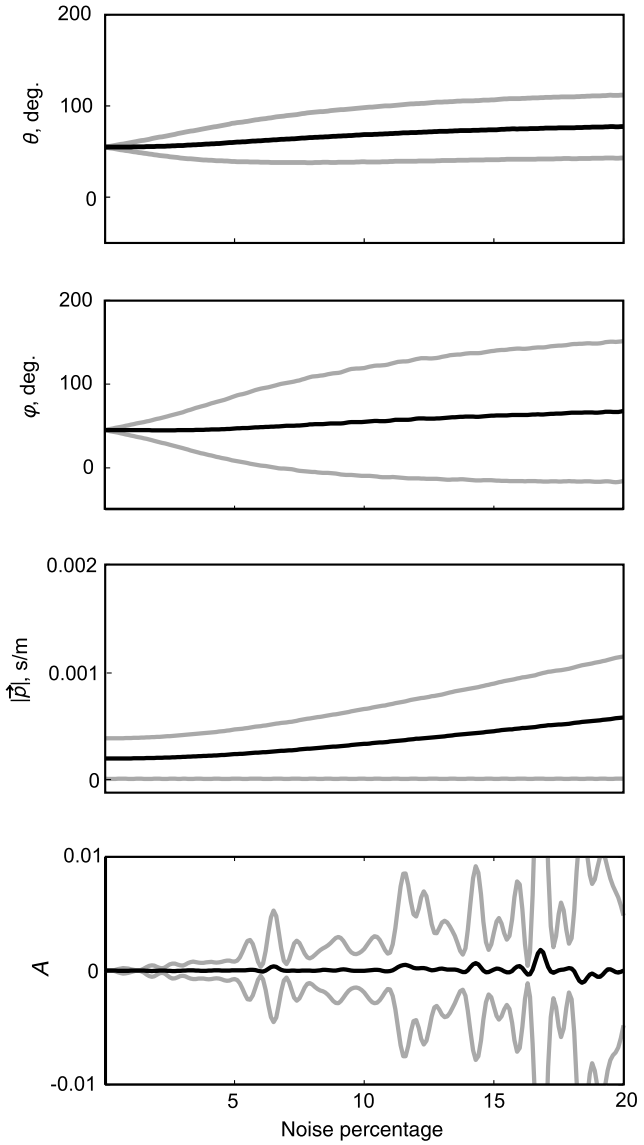

Figure 4. The result of the uncorrelated noise tests. The black line shows the mean wave attribute estimated over the time window of 60–65 s (for the same signal as shown in Fig. 3) as a function of rms noise amplitude. The gray lines show the mean variability about the mean wave attribute estimated over the same time window and is calculated as ± 1 standard deviation. The top panel shows the estimate of the wave attribute θ_s, the second panel down shows the estimate of ϕ_s, the third panel down shows the estimated wavespeed, and the bottom panel shows the geometrical spreading. As expected, increasing the rms amplitude of the noise increases the variability of the estimated wave attribute. The results shown are actually the average of one thousand individual noise realizations.

apparent in the degree of scatter at very low S_m amplitudes. Indeed, the degree of scatter in the estimate of geometrical spreading completely overwhelms the geometrical spreading estimate of the S_0 signal. It is not until the amplitude of the S_m signal surpasses ~80% that the degree of scatter decreases. At this S_m amplitude, the estimated geometrical spreading approaches that of the S_m signal itself.

In general, it appears that the estimates of the wave parameters are much more influenced by the S_m signal than the S_0 signal. This is likely because, in this case, the S_m signal is a monotonic sine wave. We find that, in general, gradiometric analysis returns wave parameters with much less scatter for this type of wavefield as opposed to a more realistic wavefield such as the synthetic seismograms seen in Figure 3. The reason for this is not clear.

Discussion and Summary

The primary goal of this paper was to develop and present the mathematical background for scalar wave gradiometry in three dimensions. We validated the methodology with synthetic data, which indicates that, in principle, 3D gradiometry is a valid process. The method can robustly return estimates of the time-variable wave direction and speed. We find, however, that the estimate of geometrical spreading is not as robust. For our tests, the wave source was located at a significant distance from the gradiometer, which would result in a negligible amount of geometrical spreading over the scale of the array. Indeed, it is well known that the geometrical spreading estimate is not robust when the seismic source is located more than a few wavelengths from the recording array (Langston, 2007c; Langston and Liang, 2008). This is a highly specific case, however, and we wished to demonstrate the more general case of a source being located far from the array. We did not attempt to estimate the radiation pattern as the problem is highly ill posed for a single gradiometer deployment. We believe, though, that it is possible in principle to estimate the radiation pattern given multiple simultaneous gradiometer deployments, and this is the subject of a forthcoming paper.

Because the analytical model assumes a source-centered coordinate system, one way to interpret a time-variable slowness vector is that the source changes positions with time. This can occur in the case of seismic scattering, where each scattering point is located in a different position, or for a finite rupture of a large fault system. Regardless, we emphasize that gradiometric analysis estimates the wave vector (and possibly the radiation patterns) of a wavefield at each time point along the seismogram. There is no inherent requirement that each seismic arrival have the same physical origin.

To test the sensitivity of wave gradiometry to random noise, we added an uncorrelated noise field to the signal and attempted to recover the known wave parameters. In general, we observed that the method is highly sensitive to uncorrelated noise. Noise acts to distort the relative amplitudes of individual wave arrivals, which are the actual observables in wave gradiometry. Because gradiometry relies on these relative amplitudes in the data, any phenomena that distorts the amplitude will significantly affect the estimation of the wave's spatial derivatives, which will affect the coefficients used to estimate the wave parameters (Suryanto *et al.*, 2006). Generally, we found that when the rms amplitude of the uncorrelated noise exceeds ~5% of the rms amplitude of

the data, the estimates of the wave parameters become unreliable. This is not an unexpected result, as previous work on 1D and 2D wave gradiometry also documented the sensitivity of the method to uncorrelated noise (Poppeliers, 2010, 2011).

In addition to investigating the effects of uncorrelated noise, we performed numerical tests where two signals with differing wave attributes interfered. For our tests, one signal took the form of simulated microseism that propagated across the array at a fixed velocity but in a direction different from that of a second, simulated earthquake signal. We found that for this test, the wave parameters estimated for the simulated earthquake signal were highly sensitive to the simulated microseism. For low microseism amplitudes ($<5\%$ of the signal amplitude), however, our method can generally recover accurate estimates of the wave direction and speed but not the geometric spreading, which displays a small but significant degree of scatter. As the amplitude of the interfering signal increases, however, the estimates of the wavespeed and direction approach that of the interfering signal itself: wave gradiometry is simply returning the estimates of the highest amplitude coherent wavefield. When the two wavefields have amplitudes within ~50% of each other, gradiometry returns results with a significant degree of scatter, to the point of being unreliable. This is not surprising, though, as at these relative amplitudes, there is effectively two equal-amplitude interfering wavefields and it is well known that wave gradiometry returns spurious results when analyzing interfering wavefields (Langston *et al.*, 2006; Langston, 2007a,b; Poppeliers, 2010, 2011). Although gradiometry offers the advantage of lower operational costs (due to the small size of the array), conventional beam-forming methods are able to discern between interfering wavefields in some cases. Gradiometry offers advantages in cost and computational speed but sacrifices some capability in such a case.

Given the results of the noise tests, it is recommended that gradiometric analysis should only be used on high-quality data. The question becomes, then, how is it known when the data is suitable? First, a quick analysis of the SNR ratio can be calculated from, for example, the pre- and the postarrival data. A second indicator as to the quality of the results can also be assessed using the multiwavelet methods presented by Poppeliers (2011). When using multiwavelet gradiometry, the relative uncertainty in the estimated wave parameters becomes quite high when significant noise is present, rendering the results useless for interpretation.

The methods developed here are suitable for any scalar wavefield recorded on a distributed 3D array. Care, however, would need to be taken to ensure that the medium in which the instruments are deployed does not contain a significant degree of spatial heterogeneity. For example, one could deploy vertical component seismometers in the appropriate geometry in a large igneous rock body. It is also possible to use the methods developed here with submerged hydrophones or airborne microphones.

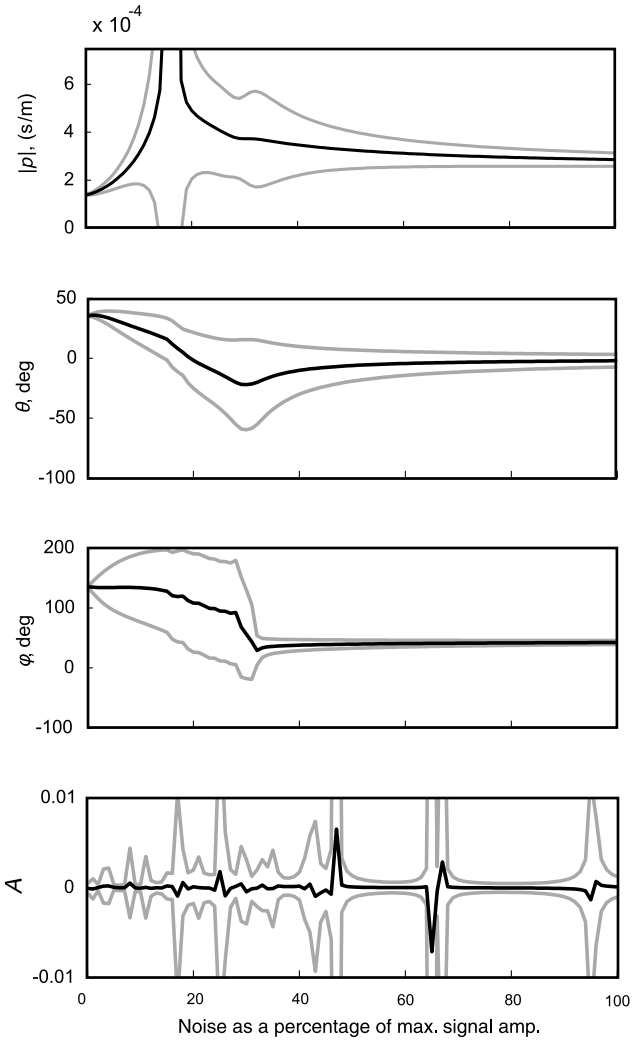

Figure 5. The effects of an interfering wavefield. The interfering wavefield is actually a monotonic sine wave the amplitude of which as a percentage of the original signal is indicated on the x axis. This interfering wavefield simulates microseism that is traveling as surface waves. The original signal is identical to that shown in Figure 3 but with constant slowness. The black line shows the mean wave attribute estimated over the time window of 60–65 s, and the gray lines show the mean standard deviation about the mean estimate over this time window. As the amplitude of the coherent noise increases, the scatter about the mean increases. As the amplitude of the coherent noise becomes larger than the signal itself, however, the scatter decreases and the estimated wave attribute approaches that of the microseism.

Data and Resources

The data used to construct the synthetic seismograms in Figures 3–5 was downloaded from the Incorporated Research Institutions for Seismology (IRIS) Data Management System and is freely available.

Acknowledgments

The authors acknowledge the very constructive and thorough comments offered by two anonymous reviewers, as well as the comments made by Associate Editor E. Chael. These reviews greatly improved the quality of this paper.

References

Earle, P. S., S. Rost, P. M. Shearer, and C. Thomas (2011). Scattered P P waves observed at short distances, *Bull. Seismol. Soc. Am.* **101,** no. 6, 2843–2854.

Frosch, R. A., and P. E. Green (1966). The concept of a large aperture seismic array, *Proc. Roy. Soc. Lond. Math. Phys. Sci.* **290,** no. 1422, 368–384.

Kay, I., S. Sol, J. M. Kendall, C. Thomson, D. White, I. Asudeh, B. Roberts, and D. Francis (1999). Shear wave splitting observations in the Archean craton of Western Superior, *Geophys. Res. Lett.* **26,** no. 17, 2669–2672.

Langston, C. A. (2007a). Spatial gradient analysis for linear seismic arrays, *Bull. Seismol. Soc. Am.* **97,** no. 1B, 265–280.

Langston, C. A. (2007b). Wave gradiometry in the time domain, *Bull. Seismol. Soc. Am.* **97,** no. 3, 926–933.

Langston, C. A. (2007c). Wave gradiometry in two dimensions, *Bull. Seismol. Soc. Am.* **97,** no. 2, 401–416.

Langston, C. A., and C. Liang (2008). Gradiometry for polarized seismic waves, *J. Geophys. Res.* **113,** no. B8, B08305.

Langston, C. A., P. Bodin, C. Powell, M. Withers, S. Horton, and W. Mooney (2006). Explosion source strong ground motions in the Mississippi embayment, *Bull. Seismol. Soc. Am.* **96,** no. 3, 1038–1054.

Liang, C., and C. A. Langston (2009). Wave gradiometry for USArray: Rayleigh waves, *J. Geophys. Res.* **114,** no. B2, B02308.

Poppeliers, C. (2010). Seismic wave gradiometry using the wavelet transform: Application to the analysis of complex surface waves recorded at the Glendora Array, Sullivan, Indiana, USA, *Bull. Seismol. Soc. Am.* **100,** no. 3, 1211–1224.

Poppeliers, C. (2011). Multiwavelet seismic-wave gradiometry, *Bull. Seismol. Soc. Am.* **101,** no. 5, 2108–2121.

Rost, S., and C. Thomas (2002). Array seismology: Methods and applications, *Rev. Geophys.* **40,** no. 3, 1008.

Selby, N. D. (2011). Improved teleseismic signal detection at small-aperture arrays, *Bull. Seismol. Soc. Am.* **101,** no. 4, 1563–1575.

Suryanto, W., H. Igel, J. Wassermann, A. Cochard, B. Schuberth, D. Vollmer, F. Scherbaum, U. Schreiber, and A. Velikoseltsev (2006). First comparison of array-derived rotational ground motions with direct ring laser measurements, *Bull. Seismol. Soc. Am.* **96,** no. 6, 2059–2071.

Department of Chemistry and Physics
Georgia Regents University
2500 Walton Way
Augusta, Georgia 30904-2200
cpoppeli@gru.edu
tamzen22@hotmail.com
(C.P., T.B.)

Department of Mathematics
Georgia Regents University
2500 Walton Way
Augusta, Georgia 30904-2200
ppunosev@gru.edu
(P.P.)

Manuscript received 3 July 2012